



Contents lists available at ScienceDirect

Medical Image Analysis

journal homepage: www.elsevier.com/locate/media

Whole myocardium tracking in 2D-echocardiography in multiple orientations using a motion constrained level-set



T. Dietenbeck^{a,*}, D. Barbosa^{a,b}, M. Alessandrini^a, R. Jasaityte^b, V. Robesyn^b, J. D'hooge^b, D. Friboulet^a, O. Bernard^a

^a Université de Lyon, CREATIS, CNRS UMR5220, INSERM U1044, Université Lyon 1, INSA-LYON, France

^b Cardiovascular Imaging and Dynamics, KU Leuven, Leuven, Belgium

ARTICLE INFO

Article history:

Received 18 February 2013

Received in revised form 8 January 2014

Accepted 24 January 2014

Available online 6 February 2014

Keywords:

Segmentation

Tracking

Active contour

Echocardiography

ABSTRACT

The segmentation and tracking of the myocardium in echocardiographic sequences is an important task for the diagnosis of heart disease. This task is difficult due to the inherent problems of echographic images (i.e. low contrast, speckle noise, signal dropout, presence of shadows). In this article, we extend a level-set method recently proposed in Dietenbeck et al. (2012) in order to track the whole myocardium in echocardiographic sequences. To this end, we enforce temporal coherence by adding a new motion prior energy to the existing framework. This motion prior term is expressed as new constraint that enforces the conservation of the levels of the implicit function along the image sequence. Moreover, the robustness of the proposed method is improved by adjusting the associated hyperparameters in a spatially adaptive way, using the available strong *a priori* about the echocardiographic regions to be segmented. The accuracy and robustness of the proposed method is evaluated by comparing the obtained segmentation with experts references and to another state-of-the-art method on a dataset of 15 sequences (≈ 900 images) acquired in three echocardiographic views. We show that the algorithm provides results that are consistent with the inter-observer variability and outperforms the state-of-the-art method. We also carry out a complete study on the influence of the parameters settings. The obtained results demonstrate the stability of our method according to those values.

© 2014 Elsevier B.V. All rights reserved.

1. Introduction

Clinical assessment of the left-ventricular function is essential for the diagnosis of heart diseases. Amongst other imaging techniques, ultrasound imaging is a popular tool since it allows real-time visualization of the heart motion through the cardiac cycle. However the extraction of functional parameters often requires a manual delineation of the heart boundaries by an expert cardiologist. The inherent problems linked to echocardiography (e.g. presence of speckle, signal dropouts) make this task prone to errors, subjective and time-consuming. In order to speed up the analysis and decrease the variability in the delineation, the automatic identification and tracking of the myocardial borders is thus a very active research area (Noble and Boukerroui, 2006; Casero and Noble, 2008; Nascimento and Marques, 2008; Carneiro et al., 2012). Despite these important research efforts, segmentation and tracking in echocardiography still face noticeable limitations: as shown in

Noble and Boukerroui (2006), most of the studies deal with the segmentation of the endocardium only and operate in one particular echocardiographic view. As a consequence, very few papers concern the tracking of the whole myocardium (Dias and Leitao, 1996; Chalana et al., 1996; Zhou et al., 2004, 2005) or of the endocardium in multiple views (Comaniciu et al., 2004; Casero and Noble, 2008). In this context, the main applicative originality of this study is the design of a methodology which allows to segment and track the whole myocardium (i.e. endo- and epicardium) in the main echocardiographic planes (i.e. parasternal short-axis, apical 4-chamber and apical 2-chamber views).

While in this work we focus on 2D segmentation, let us however note that epicardial segmentation has recently received more attention in 3D echocardiography. In Zhu et al. (2010), an incompressibility constraint was introduced in an active contour framework to segment the whole myocardium in 3D echography. In Orderud et al. (2008), coupled segmentation of endo- and epicardial borders in 3D echocardiography was performed by using a Kalman filter-based tracking framework. Although 3D imaging is receiving increasing attention, its use in clinical routine is still limited and usually coupled to 2D acquisitions which provide a better

* Corresponding author. Tel.: +33 473178449.

E-mail address: thomas.dietenbeck@creatis.insa-lyon.fr (T. Dietenbeck).

in-plane resolution. As compared to 3D, it should be noted that the segmentation and tracking of 2D echocardiographic sequences raise specific problems: the shape of the cardiac structures indeed varies considerably according to the selected echographic acquisition view, and through plane motion yields shape variations that may result in partial occlusion.

When segmenting sequences and tracking an object over time, the knowledge of the underlying motion may bring valuable information and help improving segmentation results and speed. Indeed parts of the object that are hidden in a frame might be visible in another one; temporal coherence implies that contours in successive frames have similar shapes. In the context of echocardiography, many techniques have been proposed to include the motion information in the tracking process: motion model (Chalana et al., 1996; Nascimento and Marques, 2008; Leung et al., 2011), dynamical shape priors (Bosch et al., 2002; Casero and Noble, 2008), Kalman filtering (Jacob et al., 1999; Comaniciu et al., 2004).

In Chalana et al. (1996), the authors proposed a coupled active contours technique based on snakes to segment the whole myocardium in parasternal short-axis sequences. In order to segment the myocardium over the whole sequence, the authors have suggested to minimize an energy composed of 2 terms: a gradient based term and a motion continuity term which enforces the contour to contract during systole and to expand during diastole. Nascimento and Marques (2008) presented an algorithm for the tracking of the endocardial boundary in apical 4-chamber sequences. The evolution of the shape and motion parameters is performed on an edge map using a bank of switched dynamic systems. To deal with possible outliers and multiple dynamics, a filtering algorithm was proposed, which propagates the *a posteriori* density of the unknown shape and motion parameters using a tree of probability data association filters. In the context of endocardial segmentation in 3D echocardiography, Leung et al. (2011) proposed a motion model based on PCA. After an alignment step of the dataset, Procrustes analysis is performed in order to obtain the inter-frame motion for all frames of all the sequences. The cardiac motion is modeled as an affine transformation and PCA is then applied on the affine transformation in order to learn the motion model. This PCA motion model is then introduced in the optical flow equation with the assumption that the PCA parameters are constant in small regions around the contour.

Jacob et al. (1999) incorporated shape PCA and Kalman filtering in an active contour framework. Hereto, PCA is applied to a dataset that describes heart shape variation for one specific acquisition view. The measurement step is performed using a combination of spatio-temporal noise reduction filtering and feature detection from phase information. Comaniciu et al. (2004) developed an information fusion framework to track the endocardium in parasternal short-axis and apical 4-chamber views. They formulated the tracking framework as an information fusion problem using Kalman filtering and strongly-adapted PCA and compute an uncertainty measure from the optical flow. This allows to discard flows estimated from uncertain areas such as drop-out regions while giving more importance to flows with high confidence. This technique was further extended to the tracking of the whole myocardium by Zhou et al. (2004, 2005), where the two borders were modeled as a single point in the shape space. The coupled evolution of the contours proved to be more robust in the tracking process since more information is considered in the evolution process.

Bosch et al. (2002) used an adaptation of the active appearance model (AAM) approach referred to as the active appearance motion model (AAMM) to represent the shape and appearance of the endocardium, as well as its motion. However their method was only tested on apical 4-chamber views. Casero and Noble (2008) proposed a framework to take into account the cyclic dynamics of

the heart shape. In this framework, PCA is applied on the dataset of sequences, where the pose parameters are estimated using a modified Procrustes alignment in order not to remove temporal variability inside a sequence. Temporal models of the whole myocardium in parasternal short-axis, apical 4-chamber, apical 2-chamber and apical 3-chamber views are then learned using this technique.

The main drawback of these techniques is that the motion knowledge is often learned via an interactive training process. Though this training process can take place off-line, it involves considerable effort and expertise. More importantly, since we are interested in tracking the myocardium in multiple orientations, it is difficult to make use of these approaches due to the complexity of the heart motion. It would thus require to learn a motion model per view as in Casero and Noble (2008). Furthermore, during the learning process, one has to deal with the tedious dilemma of considering both healthy and pathological subjects, since the generalization power of the statistical model depends ultimately on the database used in the training phase.

The following novelties are thus introduced in this paper.¹ We extend the previously described level-set formalism (Dietenbeck et al., 2012) to the tracking of the whole myocardium in multiple orientations (i.e. parasternal short-axis, apical 4-chamber and apical 2-chamber views). To this end, we propose to constrain the evolving contour in order to satisfy a level conservation hypothesis. This assumption ensures that the zero-level of the implicit function evolves according to the underlying motion field throughout the cardiac sequence. We then express this constraint as a motion energy and include it into the variational framework described in Dietenbeck et al. (2012). The interest of such formulation stems from the fact that this constraint does not require any learning step since we are not using a motion model. Compared to previous works that also use this assumption (Papin et al., 2000; Unal et al., 2005), our formulation is set in an energy minimization process, thus ensuring the convergence of the algorithm to a minimum. Moreover, the motion being estimated prior to the tracking, this formulation allows to choose the motion estimation algorithm that provides the best results while keeping the same tracking algorithm. Furthermore, we demonstrate the importance of this energy term by comparing tracking results with and without this term showing an improvement of the results by 25% in terms of Modified Dice, Mean Absolute Distance and Hausdorff Distance (whose definitions are given in Section 6.1).

Another novelty introduced in this article concerns the setting of the hyperparameters. Indeed, most segmentation methods formally rely on different terms reflecting the different types of information driving the segmentation process (e.g. data attachment term, shape prior, motion model, etc.). Tuning the weighting of these terms represents a difficult task and is often done empirically and in a global way. However this implies that the same weights are applied over the whole contour, in regions presenting different properties (such as different contrast) where the influence of each parameter could be needed in a different way. To tackle this problem, we propose in this paper an original approach that makes use of a very strong *a priori* about the image properties based on the heart anatomy. In this context, we introduce spatially varying parameters that allows modeling the problems linked to the different image properties depending on the position along the myocardium. More specifically, we divide each frame according to the AHA nomenclature (Cerqueira et al., 2002) and apply different weighting in each segment in order to take into account regions

¹ A preliminary version of this work appeared in Dietenbeck et al. (2013). In the present paper, we describe in detail the formal aspects of the method, propose an original way to set the weight between the different energy term. We also evaluate the performances from a data set including 900 medical images and study the robustness of the algorithm with respect to the hyperparameters.

where the data information can be trusted or in the contrary where the prior should preponderate. We then show that the use of such an anatomical prior for the hyperparameters makes the segmentation more adaptive and robust to hyperparameters changes.

The paper is organized as follows. In Section 2, we recall the general level-set framework and describe the energy functional that will be minimized. In Section 3, we detail the level conservation hypothesis and the corresponding energy term. In Section 4, we describe the setting of the hyperparameters and the image subdivision according to the anatomical properties of the sequence. Implementation issues are further discussed in Section 5. Section 6 is devoted to the results obtained from echocardiographic clinical sequences. More specifically, we compared our results with experts references and a recent method proposed by Hamou and El-Sakka (2010). We also evaluate the robustness of our algorithm with respect to the hyperparameters. We also show the generic nature of our method by applying it on 10 cardiac cine-MRI sequences and compared the obtained results with the references from one expert. The main conclusions and perspectives are given in Section 7.

2. Context

In this Section, we recall the level-set framework and the method we recently proposed for the segmentation of 2D echocardiographic images and describe the algorithm used for the motion estimation. Level-sets correspond to a class of deformable models where the shape to be recovered is captured by propagating an interface represented by the zero level-set of a smooth function which is usually called the level-set function. The evolution of the interface is generally derived through a variational formulation: the segmentation problem is expressed as the minimization of an energy functional that reflects the properties of the objects to be recovered (Osher and Sethian, 1988).

2.1. Level-set framework

Let $\Omega \in \mathbb{R}^2$ denote the image space. In the level-set formalism, the evolving interface $\Gamma \in \mathbb{R}^2$ is represented as the zero level-set of a Lipschitz-continuous function $\phi : \Omega \rightarrow \mathbb{R}$. The problem of segmenting one object from the background is then handled by the evolution of one level-set driven by the minimization of a specific energy criterion; its steady state partitions the image into two regions that delimit the boundaries of the object to be segmented.

2.2. Starting point: segmentation of echocardiographic images

In Dietenbeck et al. (2012), in order to segment 2D echocardiographic images, we proposed to minimize the following energy:

$$E = E_d + E_t + E_s, \quad (1)$$

where E_d represents the data attachment term, E_t is a term that prevents the contours from merging by imposing a minimum thickness and E_s embeds the shape prior.

2.2.1. Data attachment term

In order to cope with intensity inhomogeneities, a localized version of the Chan-Vese model (Chan and Vese, 2001; Lankton and Tannenbaum, 2008) was adopted as data attachment term E_d which can be written as

$$E_d(\phi) = \int_{\Omega} \delta(\phi(\mathbf{p})) \int_{\Omega} B(\mathbf{p}, \mathbf{q}) F(I, \phi, \mathbf{q}) d\mathbf{q} d\mathbf{p}, \quad (2)$$

where

$$F(I, \phi, \mathbf{q}) = H(\phi(\mathbf{q})) \cdot (I(\mathbf{q}) - u_x)^2 + (1 - H(\phi(\mathbf{q}))) \cdot (I(\mathbf{q}) - v_x)^2, \quad H(\cdot)$$

is the Heaviside function and $\delta(\cdot)$ is the Dirac distribution. The function $B(\cdot)$ is a binary mask corresponding to a user-defined neighborhood of point \mathbf{p} . The quantities u_x and v_x correspond to the localized version of the inside and outside average intensity values measured in the window $B(\mathbf{p})$. Minimizing E_d (2) with respect to ϕ leads to the following evolution equation:

$$f_d(\mathbf{p}) = \frac{\partial \phi}{\partial t}(\mathbf{p}) = -\delta(\phi(\mathbf{p})) \int_{\Omega} B(\mathbf{p}, \mathbf{q}) G(I, \phi, \mathbf{q}) d\mathbf{q}, \quad (3)$$

$$\text{where } G(I, \phi, \mathbf{q}) = \delta(\phi(\mathbf{q})) \left((I(\mathbf{q}) - u_x)^2 - (I(\mathbf{q}) - v_x)^2 \right).$$

2.2.2. Thickness term

Since we are dealing with the evolution of a shape bounded by two contours, they might be both attracted by the same image feature, leading to the merging of both contours. To prevent this situation, the level-set is constrained locally to have a minimum thickness R_T through the following energy:

$$E_t(\phi) = \int_{\Omega} \phi(\mathbf{p} + R_T \mathbf{N}) \cdot (1 - H(\phi(\mathbf{p} + R_T \mathbf{N}))) \cdot \delta(\phi(\mathbf{p})) d\mathbf{p}, \quad (4)$$

where \mathbf{N} corresponds to the inward normal of a point $\mathbf{p} \in \Gamma$. The evolution term is obtained by deriving the Eq. (4) with respect to ϕ and writes as:

$$f_t(\mathbf{p}) = \frac{\partial \phi}{\partial t}(\mathbf{p}) = (1 - H(\phi(\mathbf{p} + R_T \mathbf{N}))) \cdot \delta(\phi(\mathbf{p})). \quad (5)$$

2.2.3. Shape prior term

In Dietenbeck et al. (2012), the shape constraint is defined by the following shape prior energy:

$$E_s(\phi, \lambda) = \int_{\Omega} \psi^2(\mathbf{p}, \lambda) \cdot \|\nabla \phi(\mathbf{p})\| \cdot \delta(\phi(\mathbf{p})) d\mathbf{p}, \quad (6)$$

where $\psi(\mathbf{p}, \lambda)$ is the implicit function representing the distance of a point \mathbf{p} to the myocardial shape defined by two hyperquadrics of parameters λ . The minimization of (6) is addressed in a two phase scheme. First, keeping λ fixed, ϕ is evolved according to the level-set equation:

$$f_s(\mathbf{p}) = \frac{\partial \phi}{\partial t}(\mathbf{p}) = \delta(\phi(\mathbf{p})) \cdot \left(\frac{\langle \nabla \psi(\mathbf{p}, \lambda), \nabla \phi(\mathbf{p}) \rangle}{\|\nabla \phi(\mathbf{p})\|} + \psi^2(\mathbf{p}, \lambda) \cdot \kappa \right), \quad (7)$$

where κ is the curvature of the evolving interface and $\langle \cdot, \cdot \rangle$ denotes the scalar product. Then, keeping ϕ fixed, λ is updated through a least square fitting of hyperquadrics on each border.

2.3. Motion estimation

We chose to use the motion estimation technique recently proposed by Alessandrini et al. (2013). It is based on the monogenic signal which extends the concept of analytic signal to multiple dimensions (Felsberg and Sommer, 2001). The brightness consistency assumption usually used in motion estimation (Optical Flow) is replaced by a monogenic phase consistency which has proven to be more robust in ultrasound imaging. The authors proposed a multi-scale approach in order to be able to estimate large motion. The motion is assumed to be locally affine and estimated for several neighborhood size using the monogenic phase. As such, the retained displacement estimate corresponds to the one with the smallest residual error. More details on this approach could be found in Alessandrini et al. (2013).

3. Motion term

In this Section, we describe how we use the motion information to guide the evolution of the active contour. Previous studies have

generally dealt with this approach in two different ways: either considering motion as a data or as a prior knowledge.

When considering motion as a data, one can either estimate the motion prior to the segmentation (Papin et al., 2000; Unal et al., 2005; Herbulot et al., 2006) or perform a joint motion estimation and segmentation (Cremers and Soatto, 2005; Brox et al., 2006; Ehrhardt et al., 2008). In the latter, the authors usually make the assumption of the intensity conservation (optical flow OF): the intensity of an object remains constant over time. Both methods have complementary advantages and drawbacks. While relying on *a priori* estimated motion allows to select the best motion estimation algorithm independently from the segmentation approach, the joint approach allows the segmentation step to improve motion estimation and vice versa.

Another way to take advantage of the motion is to use it as a prior. In this case the constrain is implicit since motion is never estimated and never appears in the evolution equation. This prior can be introduced either through a dynamical shape prior (Cremers, 2006; Kohlberger et al., 2006; Leung et al., 2011) or by constraining the variations of the level-set function ϕ (Zhang and Pless, 2005; Lynch et al., 2008). When using dynamical shape prior, the model is often obtained through a learning step (e.g. PCA or deep learning) which can be time consuming and requires experts to manually outline the target object in a dataset. Furthermore, one has to be very careful in the dataset construction in order not to give too much weight to a particular shape while ensuring that the training set is representative enough to cope with the variability of the shapes to be segmented. Finally, in contrary to the myocardial borders where geometrical prior could be used, the heart motion is difficult to model through mathematical functions and it would thus require to learn a motion model per view as in Casero and Noble (2008). Note that some authors (Zhu et al., 2010; Lynch et al., 2008) proposed to use a framework based on the incompressibility constraint but this prior cannot be used in our case since we are working in 2D and not in 3D.

Therefore, we have chosen to consider motion as information and assume it has been estimated prior to segmentation. Indeed this solution is flexible since at any time, we can select the motion estimation method that produces the best results, while keeping the same tracking algorithm which will be described in the sequel.

3.1. Energy formulation

The proposed motion term enforces the conservation of the level of the implicit function along the sequence. This can be written as

$$\phi_x u + \phi_y v + \phi_t = 0 \iff \nabla \phi \cdot \mathbf{V} = 0, \quad (8)$$

where ϕ is the level-set, $\nabla = (\partial/\partial x, \partial/\partial y, \partial/\partial t)$, $\phi_x = \partial\phi/\partial x$ and $\mathbf{V} = (u, v, 1)$ is the motion expressed in homogeneous coordinates.

This constraint is then expressed as an energy in a variational formalism as follows:

$$E_m(\phi) = \frac{1}{2} \int_{\Omega} (\nabla \phi(\mathbf{p}) \cdot \mathbf{V}(\mathbf{p}))^2 d\mathbf{p} \quad (9)$$

in order to impose the level conservation hypothesis (8). Indeed one can clearly see that the minimum of (9) is achieved when the levels of ϕ satisfy the constraint.

Note however that if we minimize the energy (9), we will not be able to keep the signed distance property for ϕ and thus may have numerical instabilities. To tackle this problem, we note that we only need the zero-level of ϕ to satisfy the level consistency assumption. Thus we rewrite (9) as:

$$E_m(\phi) = \frac{1}{2} \int_{\Omega} \delta(\phi(\mathbf{p})) (\nabla \phi(\mathbf{p}) \cdot \mathbf{V}(\mathbf{p}))^2 d\mathbf{p}, \quad (10)$$

where $\delta(\cdot)$ is the Dirac distribution allowing to consider only the zero-level of ϕ . As detailed in the sequel, we reinitialize periodically ϕ to a signed distance map (Osher and Fedkiw, 2002).

The evolution equation is obtained by minimizing (10) with respect to ϕ and is given by:

$$f_m(\mathbf{p}) = \frac{\partial \phi}{\partial \tau}(\mathbf{p}) = \delta(\phi(\mathbf{p})) (\mathbf{V}^T \mathcal{H}(\phi) \mathbf{V} + \nabla \phi^T \mathcal{J}(\mathbf{V}) \mathbf{V} + \text{Tr}(\mathcal{J}(\mathbf{V})) \nabla \phi^T \mathbf{V}), \quad (11)$$

where $\mathcal{H}(\phi)$ is the Hessian matrix of ϕ , $\mathcal{J}(\mathbf{V})$ the Jacobian matrix of \mathbf{V} and $\text{Tr}(A)$ is the trace of the matrix A . τ is an artificial time parameter that does not correspond to the “real” time dimension t . Note that the complete derivation is given in Appendix A.

To segment complete echocardiographic sequences, we propose to add the motion term (10) to the energy (1) described in Dietenbeck et al. (2012) yielding the following general expression for the energy:

$$E = v_d E_d + v_t E_t + v_s E_s + v_m E_m, \quad (12)$$

where E_d represents the chosen data attachment term (2), E_t is the anti-collision term (4), E_s embeds the shape prior (6) and E_m is the motion term (10). v_i with $i = \{d, s, t, m\}$ are hyperparameters weighting the influence of the different terms.

The level-set then evolves according to the following equation:

$$\frac{\partial \phi}{\partial \tau}(\mathbf{p}) = v_d f_d(\mathbf{p}) + v_t f_t(\mathbf{p}) + v_s f_s(\mathbf{p}) + v_m f_m(\mathbf{p}), \quad (13)$$

where $f_d(\cdot)$ is the data attachment term given in Eq. (3), $f_s(\cdot)$ is the shape prior term given in Eq. (5), $f_t(\cdot)$ is the thickness term given in Eq. (7) and $f_m(\cdot)$ is the motion term given in Eq. (11).

3.2. Implementation of the evolution equation

In order to avoid numerical instabilities, the derivatives of ϕ should be computed using Upwind schemes (Osher and Sethian, 1988). Considering (11), it can be seen that we have to compute the first and second order derivatives of ϕ with respect to each dimension (x, y and t). Spatial derivatives can be easily computed though one may need to impose boundary conditions in order to compute the backward/forward derivatives on $\partial\Omega$. On the other hand, temporal derivatives (forward and 2nd order) require to use $\phi(t+1)$ which is not available when segmenting the frame t .

A first solution would be to segment the whole sequence considering a 3D level-set: $\phi: \mathbb{R}^2 \times \mathbb{R}^+ \mapsto \mathbb{R}$. However, this solution has several drawbacks. First, due to the local nature of the data attachment term, the initial contour on each frame has to be close to the true myocardial boundaries. However, such an initialization is not a trivial task when considering 2D echocardiographic sequences. A second drawback is that we would need to acquire the complete sequence before being able to process it making the algorithm not usable for on-line analysis.

This issue is solved by computing an approximation of ϕ at t and $t+1$ from the knowledge of $\phi(t-1)$ and the available motion field: starting from the segmentation result at $t-1$, we extract the points belonging to the myocardial boundary and track them using the estimated motion at $t-1$ and t to obtain the predicted contour at $t+1$. From this contour, a signed distance map is computed and used for the derivatives computation.

Note that the first derivatives of the velocity \mathbf{V} are computed using standard centered derivatives. This only implies that we need to compute the motion at time $t+1$ as well.

4. Spatially varying hyperparameters

A common problem of active contour methods is the setting of the hyperparameters weighting the different energy terms and

their evaluation. Indeed, their values are often chosen empirically in order to give the same importance to all the terms or in the contrary to let one term preponderate over all the others. However, in echocardiography, it is interesting to vary the parameter influence according to some image information. Indeed in regions with a good contrast (e.g. area 1 in Fig. 1(c), area 2 in Fig. 1(f)), one may trust the data information and thus drastically decrease the weight of the shape prior one. Inversely, in regions where the object is not clearly visible (e.g. area 1 in Fig. 1(f)), the shape prior should be more important than the data information in order to keep meaningful results.

A first way to adjust the hyperparameters, would be to use an uncertainty measure as proposed by some authors (Comaniciu et al., 2004; Zhou et al., 2004, 2005; Bruhn and Weickert, 2006; Brox et al., 2010). In Comaniciu et al. (2004) and Zhou et al. (2004, 2005), this measure is derived from the motion estimated through optical flow in an information fusion context. Bruhn and Weickert (2006) proposed to use the inverse contribution of a point to the motion estimation energy as a confidence measure at this point. Thus a point satisfying the conditions imposed by the minimized energy will have a high confidence value and conversely. Brox et al. (2010) further extended this work to combine the information from 3 different trackers. In addition to the point correspondences obtained through motion estimation, SIFT and active contours were also used to track the position of an object. The confidence in the active contour result was obtained by considering the difference of log-likelihood within a small region around a point. Indeed since the algorithm tries to maximize this difference, a low confidence value should be given to points where it is close to 0. However, designing such an uncertainty measure for echocardiography raises several difficulties, linked to the specificities of the cardiac images and the segmentation task. First, when segmenting the parasternal short-axis view, the papillary muscles (area 2 in Fig. 1(c)) have to be excluded from the segmen-

tation although they share similar intensity properties with the myocardium (Duan et al., 2010). Thus the data information should not be taken into account in this region despite the good contrast with respect to the blood pool. Such behavior clearly corresponds to *a priori* information and thus cannot be reflected through image-based confidence measures. Moreover, since we are interested in segmenting the whole myocardium in multiple orientations, another difficulty corresponds to the fact that image properties are not the same if the endocardial or epicardial border is considered. Indeed when segmenting the endocardium, the intensity of the myocardial muscle is generally higher than the one of the blood pool (area 1 in Fig. 1(c)). However, if we consider the epicardium, we can have areas where the myocardium is brighter than surrounding tissue (area 2 in Fig. 1(f)) or in the contrary darker (area 3 in Fig. 1(c)). In order to cope with these difficulties we propose a solution consisting in building and using an *a priori* defined from the anatomical knowledge and image formation, as detailed in the following.

To tackle this problem, we take advantage of the available strong *a priori* about the echocardiographic regions to be segmented, in order to adjust the associated hyperparameters in a spatially adaptive way. We propose to divide each frame in regions with different image properties according to a generic anatomic model designed for echocardiography. This division is indeed based on the AHA nomenclature (Cerqueira et al., 2002) and shown in Fig. 1. Each segment is then classified into one of three predefined region:

- Balanced (BA): same importance is given to all terms. The weights are thus all set to 1.
- Motion dominant (MD): more importance is given to the motion term than to the shape prior. To this end, v_m is increased by 50% and v_s is decreased by 50% with respect to the value of the balanced region.

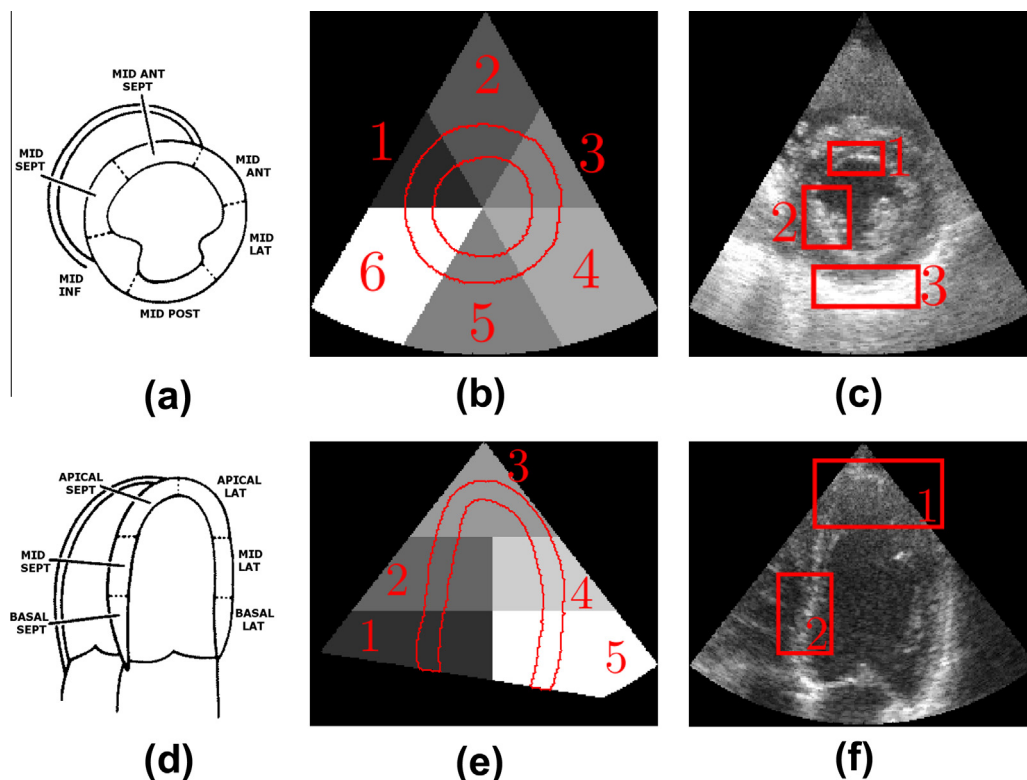


Fig. 1. Spatial division of the image. Top row: parasternal short-axis view, bottom row: apical views. (a), (d) AHA nomenclature (from Cerqueira et al., 2002); (b), (e) spatial division of the hyperparameter map with a reference contour in red; (c), (f) corresponding frame.

- Shape dominant (SD): the shape prior should preponderate over the other terms. Similarly to the MD region, v_s is increased by 50% and v_d is decreased by 50% with respect to the value of the balanced region.

The set of parameters (v_d, v_s, v_m) corresponding to this classification is given in Table 1. Note that the hyperparameter of the thickness term v_t is still set in a global way. Indeed, the thickness term is used to avoid merging situation and should thus preponderate regardless of the region properties.

The labeling of a region as BA, MD or SD follows well accepted *a priori* knowledge on how US image contents varies in clinical data. For example, the segmentation of the apex (region 3 in Fig. 1(d)) or the papillary muscles (region 4 to 6 in Fig. 1(b)) requires the use of a strong shape prior because of the absence or of misleading image information. These regions are thus considered as shape dominant. On the other hand, regions such as the septum (region 1 and 2 in Fig. 1(d)) or the anteroseptal wall (region 2 in Fig. 1(b)) offer a good contrast between the myocardium and surrounding tissue or the blood pool and are thus labeled as motion dominant.

Table 2 summarizes for each border and each region the corresponding classification. The stability of the segmentation results with respect to these parameters is moreover quantitatively studied in Section 6.4.

5. Implementation issues

5.1. Level-set evolution

The implicit function is represented by a signed distance function ϕ and is re-initialized every iteration using a fast marching scheme (Sussman et al., 1998). In order to improve efficiency, we only compute values of ϕ in a narrow band around the zero level-set. The neighborhood $B(\mathbf{p})$ defining the localization of the data attachment term is chosen in our case as a circular neighborhood, with radius R_N chosen as the average half thickness of the myocardium, i.e. 8 pixels in our case. In the same way, the value of R_T in the thickness term (4) was chosen to be set to 5 pixels. The justification of these values can be found in Dietenbeck et al. (2012). The hyperparameters weighting the different evolution terms (given in Table 1 and 2) are kept fixed in all experiments.

The following procedure is used to initialize the algorithm:

- The user is asked to input 5 points on the epicardium and 1 on the endocardium from which two concentric ellipses are fitted.
- The algorithm described in Dietenbeck et al. (2012) is used to segment the first frame of the sequence.

Table 1
Value of the hyperparameters according to the segment classification.

	Motion dominant	Balanced	Shape dominant
v_d	1	1	1/2
v_s	1/2	1	3/2
v_m	3/2	1	1

Table 2

Type of region for each view and border. The number attributed to a region correspond to the number given in Fig. 1. MD: motion dominant region; BA: balanced region; SD: shape dominant region.

Region	Parasternal short-axis view						Apical views				
	1	2	3	4	5	6	1	2	3	4	5
Endocardium	BA	MD	BA	SD	SD	SD	MD	MD	SD	BA	MD
Epicardium	BA	MD	BA	BA	MD	BA	BA	BA	SD	BA	BA

- The subsequent frames are then automatically segmented using the proposed algorithm.

Note that for the first frame of the sequence, the motion information is not available and we thus use the algorithm proposed in Dietenbeck et al. (2012) for the segmentation of one image. For the subsequent frames, the motion can be estimated using the method of Alessandrini et al. (2013) and all terms are then considered in the evolution equation (as given in Eq. (13)).

5.2. Creation of a dynamic ROI in apical views

When dealing with apical views, we proposed in Dietenbeck et al. (2012) to define a region of interest (ROI) where the myocardium may be present in the image. Since we are dealing with sequences, we need to update this ROI in order to make it correspond to the part of the image where the myocardium is visible. This task is performed as follows:

1. the 4 intersection points \mathbf{p}_t between the segmentation result and the ROI at time t are computed (green points in Fig. 2(a) and (b));
2. the estimated motion is applied to these points to get their approximate position at $t + 1$ denoted as \mathbf{p}_{t+1} (yellow points in Fig. 2);
3. least square fitting is used to estimate the closest line to \mathbf{p}_{t+1} (blue line in Fig. 2(c));
4. a mask is created and used as a ROI at $t + 1$.

This procedure is illustrated in Fig. 2.

6. Experiments

6.1. Comparison protocol

6.1.1. Experimental data

The reference dataset is composed of 15 echocardiographic sequences (5 per view) acquired from 11 healthy volunteers. The sequences were recorded using a GE Vivid E9 system equipped with a 2.5 MHz M5S probe (GE Vingmed Ultrasound, Horten, Norway). Two experts manually outlined the myocardium on one cardiac cycle per sequence resulting in the following reference distribution:

- 290 frames in parasternal short-axis view,
- 300 frames in apical 4-chamber view,
- 300 frames in apical 2-chamber view.

6.1.2. Error measures

To evaluate the accuracy of the algorithm, we measured the correspondence between the tracking results and the mean myocardial shape of the two experts contour obtained using the procedure described in Chalana and Kim (1997). In particular we adopt three different metrics, i.e. the modified Dice coefficient D^* (Dice, 1945), the Mean Absolute Distance MAD (expressed in mm) (Comaniciu et al., 2004) and the Hausdorff distance HD (expressed in mm) (Huttenlocher et al., 1993). If we call with R

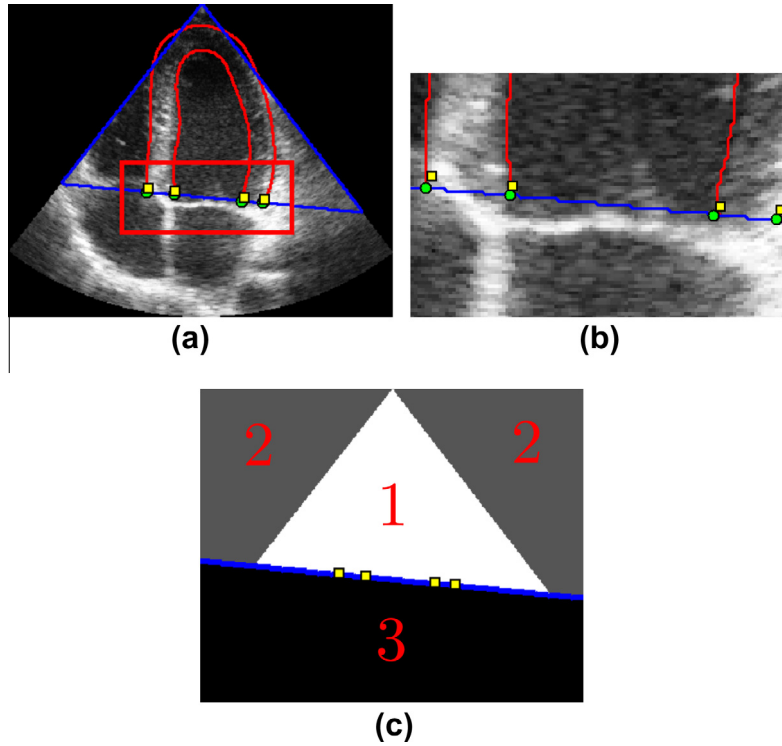


Fig. 2. Example of a tracking of the ROI: (a) the image at t . Red: segmentation result; Blue: ROI; Green dots: \mathbf{p}_i ; Yellow dots: \mathbf{p}_{i+1} (b) Zoom of the region delineated red in (a). (c) ROI at $t + 1$; Yellow dots: \mathbf{p}_{i+1} ; Blue: closest line to \mathbf{p}_{i+1} . (For interpretation of the references to colour in this figure legend, the reader is referred to the web version of this article.)

and S the reference contour and the fitted one, and introduce the generic points \mathbf{r} and \mathbf{s} belonging to R and S respectively, then the Mean Absolute Distance and the Hausdorff distance are defined as:

$$MAD(R, S) = \frac{1}{T} \sum_{t=1}^T \frac{1}{N_S} \sum_{\mathbf{s} \in S(t)} |d(\mathbf{s}, R(t))| \quad (14)$$

and

$$HD(R, S) = \frac{1}{T} \sum_{t=1}^T \max \left(\sup_{\mathbf{r} \in R(t)} d(\mathbf{r}, S(t)); \sup_{\mathbf{s} \in S(t)} d(\mathbf{s}, R(t)) \right), \quad (15)$$

where $d((p), A)$ is the Euclidian distance from a point \mathbf{p} to the curve A and T is the number of frames in a given sequence. By defining Ω_R and Ω_S as the sets of pixels within the segmented and the reference region, the modified Dice coefficient is given by:

$$D^*(\Omega_R, \Omega_S) = \frac{1}{T} \sum_{t=1}^T \left(1 - \frac{2 \text{Area}(\Omega_S(t) \cap \Omega_R(t))}{\text{Area}(\Omega_R(t)) + \text{Area}(\Omega_S(t))} \right). \quad (16)$$

Moreover, the Williams test (Chalana and Kim, 1997) was used to assess whether the results from our algorithm are within the agreement limits of the experts' manual references. When the Williams index (WI) is greater or equal to one, it indicates that our tracking results differ from the manual references as much as they differ from one expert to another. In fact, whenever the upper bound of the 95% confidence interval of the WI ($WI_{95\%}$) is greater than one, there is no statistical evidence that the agreement between our method and the reference observers is less than the reference interobserver agreement. Further details regarding this test can be found in the original work of Chalana and Kim (1997).

The method is also compared with a recent algorithm proposed by Hamou and El-Sakka (2010). This method is close to ours since it uses both a motion and a shape term in a GVF-based snake framework. More specifically two edge maps are computed and used alternatively to evolve the curve: the first one is based on the opti-

cal flow computed between two subsequent frames while the second one is a shape prior based on 3rd order hyperbolas. The parameters of the method were set to the value given by the authors in their article.

6.2. Importance of the motion information

In order to show the efficiency of motion information in improving segmentation results, we segmented the whole dataset using three different methods:

1. Pure tracking: the contour points are displaced using the estimated motion to track the myocardial border.
2. Multistatic segmentation: the algorithm described in Dietenbeck et al. (2012) is used successively on each frame. The initial contour at $t + 1$ corresponds to the contour obtained after tracking of the segmentation result t .
3. Our proposed method.

In all the methods, the monogenic motion estimation described in Section 2.3 was used. The results obtained on the whole dataset using these methods are given in Table 3 and a Friedman rank test ($p < 0.005$, Chalana and Kim, 1997) was applied to compare the results obtained using the proposed method and the two other ones.

From these figures, we can see that the proposed method outperforms the multistatic one because of the use of the motion term which imposes a temporal coherence in the tracking. Indeed, the motion can provide reliable information to follow moving structures or intensity changes in structures. Since this information is not taken into account in the static segmentation algorithm described in Dietenbeck et al. (2012), the proposed method manages to segment these structures more robustly. Compared to the tracking algorithm, our method provides better results for all measures with differences that are statistically significant. This improvement

Table 3

Results of the tracking of the myocardial border on the whole dataset in term of modified Dice criterion (D^*), Mean Absolute Distance (MAD) and Hausdorff distance (HD). The values are given as mean (Standard deviation). HD and MAD are given in mm.

	Epicardium			Endocardium		
	D^*	MAD	HD	D^*	MAD	HD
Tracking	3.57×10^{-2} (1.41×10^{-2})	1.35^\dagger (0.545)	4.38^\dagger (1.73)	5.85×10^{-2} (2.14×10^{-2})	1.47^\dagger (0.583)	4.4^\dagger (1.7)
Multistatic segmentation	13.4×10^{-2} (12.1×10^{-2})	4.41^\dagger (3.76)	12.9^\dagger (10.6)	17×10^{-2} (14.6×10^{-2})	4.09^\dagger (3.2)	12.9^\dagger (11.1)
Proposed method	3.11×10^{-2} (1.68×10^{-2})	1.16 (0.577)	3.48 (1.54)	5.19×10^{-2} (2.26×10^{-2})	1.33 (0.625)	3.68 (1.51)

[†] The difference was found significant ($p < 0.005$) when compared to the proposed method.

Table 4

Results of the segmentation of the epicardial border. The results of our method and the one described in Hamou and El-Sakka (2010) as well as the Inter-Observers Distance (IOD) are shown in term of modified Dice criterion (D^*), Mean Absolute Distance (MAD) and Hausdorff distance (HD). The values are given as mean (Standard deviation). HD and MAD are given in mm.

	IOD			Our method			Hamou		
	D^*	MAD	HD	D^*	MAD	HD	D^*	MAD	HD
Parasternal short-axis	2.71×10^{-2} (1.17×10^{-2})	0.77 (0.34)	2.30 (0.77)	3.76×10^{-2} (1.64×10^{-2})	1.07 (0.49)	2.96 (1.10)	$9.43 \times 10^{-2}^\dagger$ (9.60×10^{-2})	2.48^\dagger (2.45)	5.72^\dagger (4.53)
Apical 4-chamber	3.22×10^{-2} (1.12×10^{-2})	1.50 (0.52)	4.27 (1.49)	2.92×10^{-2} (1.69×10^{-2})	1.25 (0.63)	3.84 (1.64)	$10.6 \times 10^{-2}^\dagger$ (7.16×10^{-2})	4.02^\dagger (2.48)	10.1^\dagger (6.1)
Apical 2-chamber	3.47×10^{-2} (1.10×10^{-2})	1.54 (0.41)	3.78 (0.97)	2.67×10^{-2} (1.52×10^{-2})	1.15 (0.59)	3.62 (1.65)	$8.59 \times 10^{-2}^\dagger$ (6.78×10^{-2})	3.28^\dagger (2.14)	7.69^\dagger (4.97)

[†] The difference was found significant ($p < 0.005$) when compared to our method.

Table 5

Results of the segmentation of the endocardial border. The results of our method and the one described in Hamou and El-Sakka (2010) as well as the Inter-Observers Distance (IOD) are shown in term of modified Dice criterion (D^*), Mean Absolute Distance (MAD) and Hausdorff distance (HD). The values are given as mean (Standard deviation). HD and MAD are given in mm.

	IOD			Our method			Hamou		
	D^*	MAD	HD	D^*	MAD	HD	D^*	MAD	HD
Parasternal short-axis	7.32×10^{-2} (3.17×10^{-2})	1.53 (0.70)	3.38 (1.23)	5.03×10^{-2} (1.85×10^{-2})	0.99 (0.36)	2.66 (0.87)	$10 \times 10^{-2}^\dagger$ (10.1×10^{-2})	1.81^\dagger (1.62)	4.27^\dagger (3.44)
Apical 4-chamber	6.33×10^{-2} (2.80×10^{-2})	1.80 (0.76)	4.86 (1.54)	5.61×10^{-2} (2.31×10^{-2})	1.61 (0.66)	4.31 (1.44)	$13.3 \times 10^{-2}^\dagger$ (7.09×10^{-2})	3.63^\dagger (1.67)	10.8^\dagger (5.69)
Apical 2-chamber	5.53×10^{-2} (1.87×10^{-2})	1.57 (0.47)	3.89 (0.88)	4.93×10^{-2} (2.51×10^{-2})	1.39 (0.64)	4.02 (1.58)	$12.2 \times 10^{-2}^\dagger$ (13.5×10^{-2})	3.33^\dagger (3.15)	9.94^\dagger (9.22)

[†] The difference was found significant ($p < 0.005$) when compared to our method.

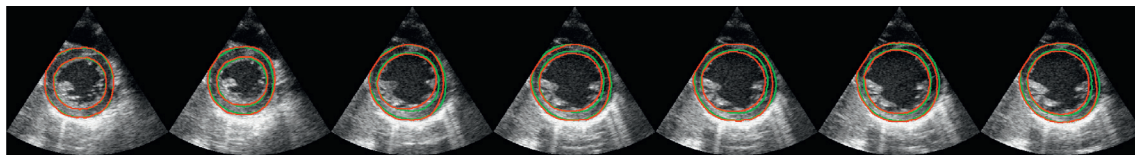
is particularly pronounced for the Hausdorff distance (HD) which is improved by 1 mm and 0.7 mm for the epicardium and the endocardium respectively. This is due to the fact that our method has the advantage of using more information (i.e. intensity and shape) which allows it to deal better with areas where the motion is not a source of reliable information (such as low contrast or near-field areas).

6.3. Myocardial tracking results

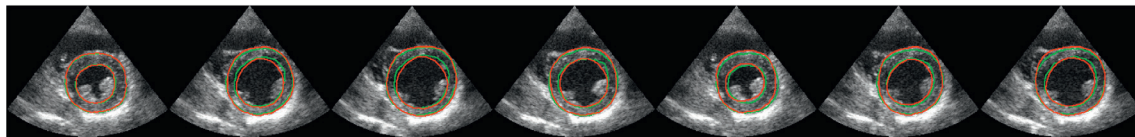
We evaluate in this section the performance of our segmentation algorithm. The comparison protocol is the one described in 6.1 and the inter-observer distance (IOD) reported in the tables corresponds to the mean of the distances computed between the references of each expert. Tables 4 and 5 provide the mean and standard deviation of the error measures obtained for the complete data set on epicardial and endocardial borders, respectively. In each table, we give for each measure (D^* , MAD, HD) the IOD (three first columns), the error measures associated to the proposed method (three middle columns) and to Hamou's method (three last

columns). To illustrate the quality of our results, we show examples of good tracking results and the associated mean reference contour of the cardiologists for parasternal short-axis (Fig. 3) and apical (Fig. 4 and 5) views. We also give some of the worst tracking results we obtained in Fig. 6 as well as the experts references on these images.

Considering, in a first step, the segmentation of the epicardium in parasternal short-axis view (first line in Table 4, Fig. 3), it may be observed that our method provides small values for all the criteria ($D^* = 3.76 \times 10^{-2}$, MAD = 1.07 mm and HD = 2.96 mm). This means that our segmentation results are close to the reference contours both on a global (D^* and MAD) and a local (HD) scale for this orientation. When compared to the corresponding IOD (three first columns in Table 4), it may be observed that the values obtained with the proposed method are close but slightly higher than the inter-observer ones (2.71×10^{-2} , 0.77 mm and 2.3 mm for the modified Dice, the MAD and the HD respectively). This indicates that the segmentation provides consistent results in the sense that the difference with the experts reference is comparable to the distance between experts.

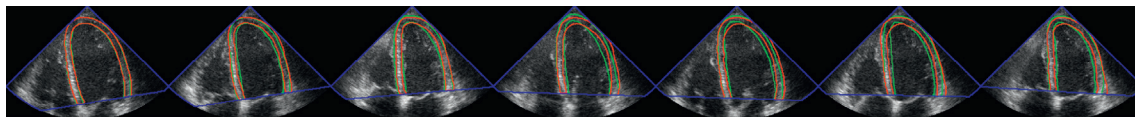


(a) Endocardium: 1.09mm (2.48mm); Epicardium: 0.84mm (2.29mm)

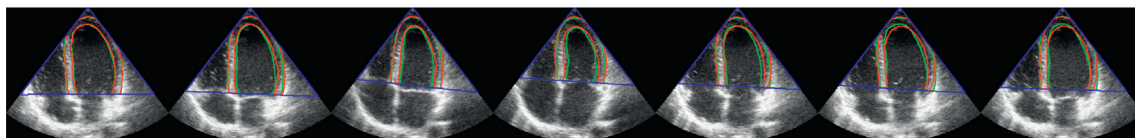


(b) Endocardium: 1.17mm (3.25mm); Epicardium: 0.92mm (2.54mm)

Fig. 3. Results of the tracking of the whole myocardium at 7 time points in the cardiac cycle in parasternal short-axis views. Green: mean reference of the cardiologists; Red: our contour. For each sequence, the MAD (HD) computed between the segmentation result and the mean contour is given. (For interpretation of the references to colour in this figure legend, the reader is referred to the web version of this article.)

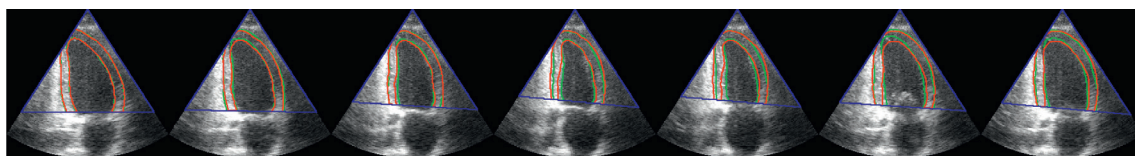


(a) Endocardium: 1.87mm (4.15mm); Epicardium: 1.13mm (3.28mm)

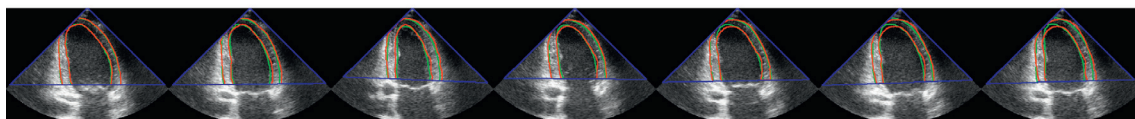


(b) Endocardium: 1.73mm (3.99mm); Epicardium: 0.93mm (2.78mm)

Fig. 4. Results of the tracking of the whole myocardium at 7 time points in the cardiac cycle in apical 4-chamber views. Green: mean reference of the cardiologists; Red: our contour and Blue: region of interest. For each sequence, the MAD (HD) computed between the segmentation result and the mean contour is given. (For interpretation of the references to colour in this figure legend, the reader is referred to the web version of this article.)



(a) Endocardium: 1.43mm (4.61mm); Epicardium: 1.03mm (3.19mm)



(b) Endocardium: 1.24mm (3.98mm); Epicardium: 1.14mm (4.51mm)

Fig. 5. Results of the tracking of the whole myocardium at 7 time points in the cardiac cycle in apical 2-chamber views. Green: mean reference of the cardiologists; Red: our contour and Blue: region of interest. For each sequence, the MAD (HD) computed between the segmentation result and the mean contour is given. (For interpretation of the references to colour in this figure legend, the reader is referred to the web version of this article.)

The results associated with the endocardial borders in the same parasternal short-axis view (first line in Table 5), show that the errors are in the same order and slightly lower: 5.03×10^{-2} for the modified Dice, 0.99 mm for the MAD and 2.66 mm for the HD. This shows that due to the spatially varying weighting, we are able to deal with both highly and poorly contrasted regions. Indeed, in the septum, anteroseptal and anterior walls, the contrast between

the myocardium and the blood pool is usually high and we thus set a higher importance to the data attachment term and the motion term than to the shape prior. On the other hand, the papillary muscle present intensity properties similar to the myocardium making them difficult to separate using the data attachment term. Moreover they also have a through-plane motion which means that they may not be present during the whole sequence. This, in turn, may

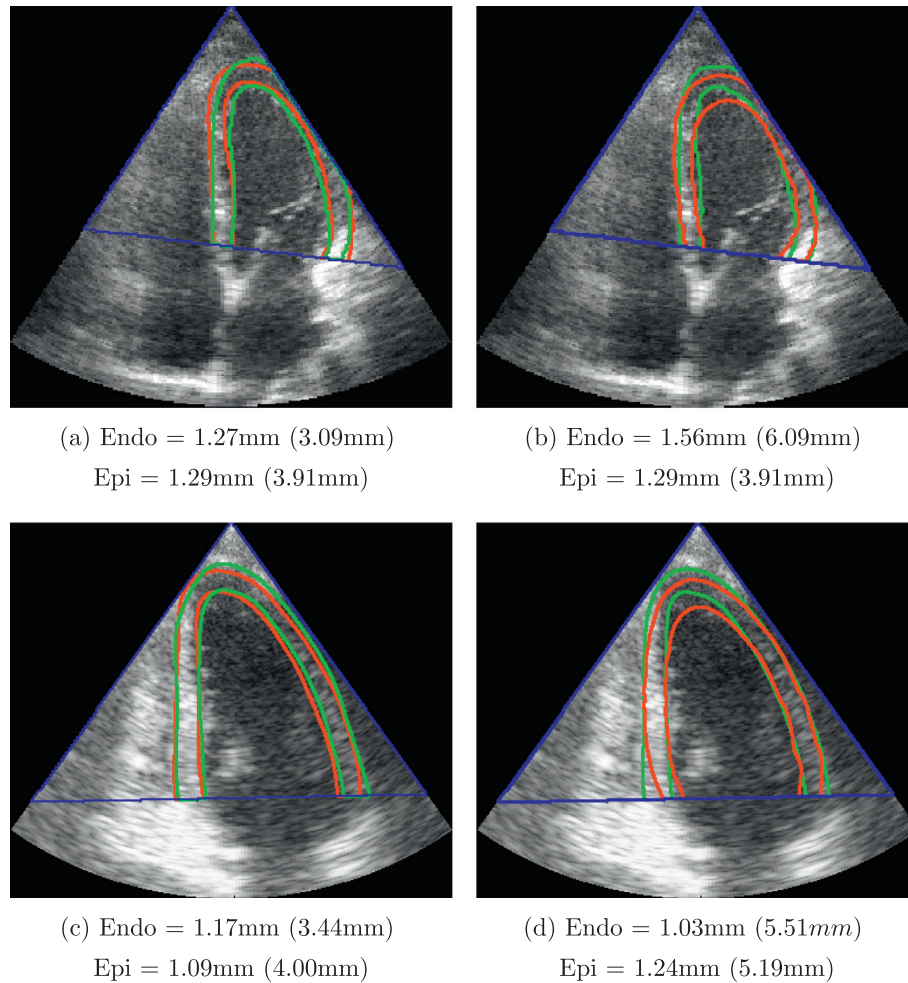


Fig. 6. Example of some of the worst case of tracking of the whole myocardium. Left column: references of the two experts; Right column: tracking result with our contour in red, the mean cardiologist in green and the region of interest in blue. For each image, the MAD (HD) computed between the two experts references or between the segmentation result and the mean contour is given. (For interpretation of the references to colour in this figure legend, the reader is referred to the web version of this article.)

Table 6
Williams Index (IW) and Confidence Interval (CI) for the epicardial border.

	D^*		MAD		HD	
	WI	CI	WI	CI	WI	CI
Parasternal short-axis	0.734	[0.731; 0.736]	0.729	[0.727; 0.731]	0.755	[0.754; 0.757]
Apical 4-chamber	0.946	[0.942; 0.949]	0.989	[0.985; 0.993]	0.939	[0.936; 0.941]
Apical 2-chamber	1.187	[1.184; 1.190]	1.215	[1.212; 1.219]	0.938	[0.935; 0.941]

Table 7
Index of Williams (IW) and Confidence Interval (CI) for the endocardial border.

	D^*		MAD		HD	
	IW	CI	IW	CI	IW	CI
Parasternal short-axis	1.045	[1.041; 1.048]	1.074	[1.071; 1.078]	0.99	[0.987; 0.992]
Apical 4-chamber	1.077	[1.074; 1.080]	1.060	[1.058; 1.063]	1.003	[1; 1.006]
Apical 2-chamber	1.11	[1.107; 1.113]	1.108	[1.105; 1.111]	0.916	[0.913; 0.919]

imply a wrong motion estimation when these structures (dis)appear, making them difficult to follow with the motion term. By letting the shape prior preponderate in this region, we are thus able to cope with these difficulties. Note also that our results are still in the same order and slightly lower than the corresponding IOD

(7.32×10^{-2} for D^* , 1.53 mm for the MAD and 3.38 mm for the HD).

If we now consider the other views (two last lines of Tables 4 and 5), we observe that in the parasternal short-axis view, the myocardium is better tracked than in apical views (e.g. the MAD

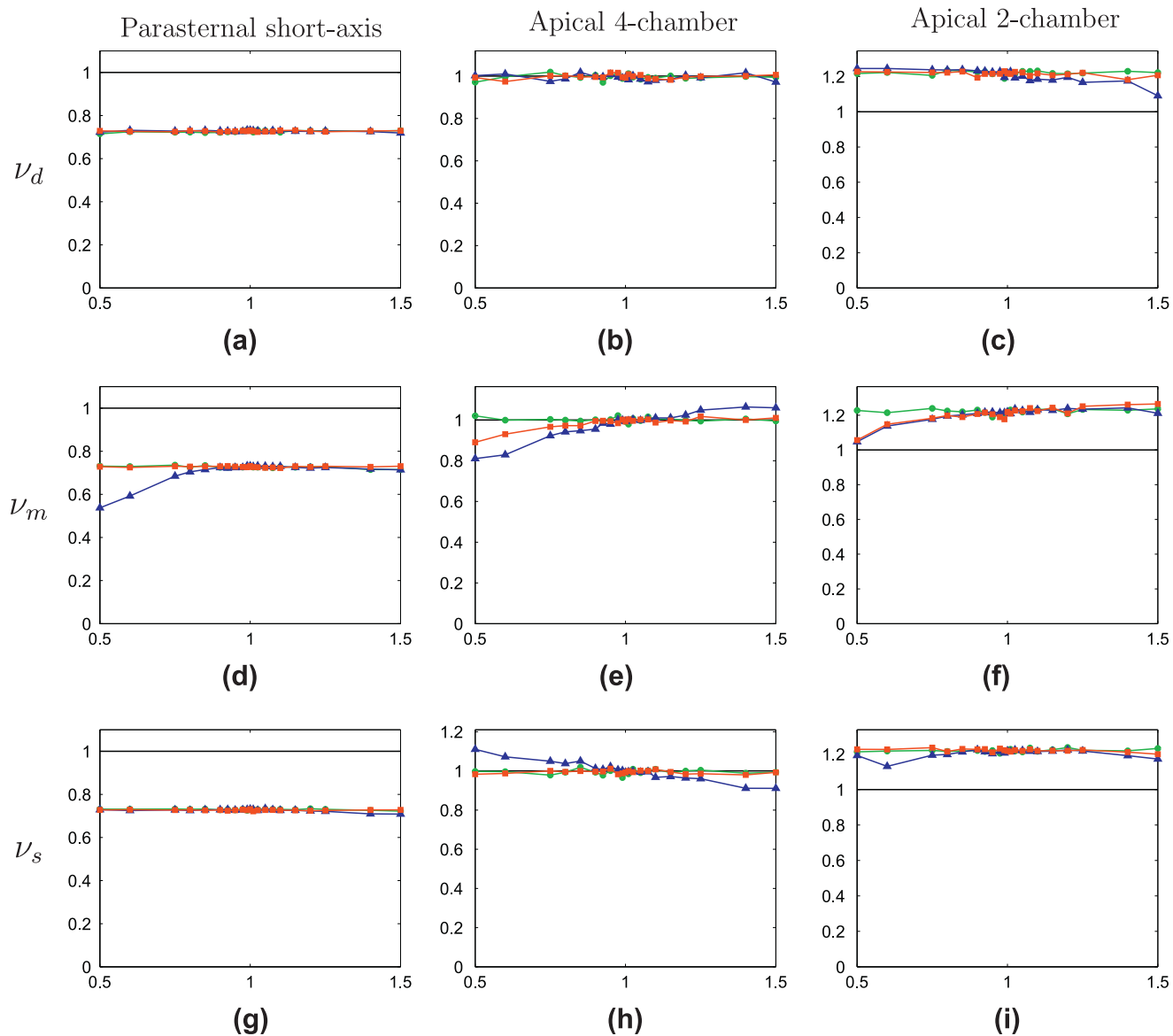


Fig. 7. Influence of the algorithm's parameters variation on the epicardial tracking performance. On the x-axis, 1 corresponds to the nominal value of the parameter and 0.5 (resp. 1.5) corresponds to a variation of -50% (resp. 50%) of the nominal value. Green: Data dominant region; Blue: Balanced region; Red: Shape dominant region. (For interpretation of the references to colour in this figure legend, the reader is referred to the web version of this article.)

for the endocardial border is 0.7 mm smaller in parasternal short-axis than in apical 4-chamber view). This can be explained by a better image quality achieved in parasternal views, where the myocardium is well-defined. On the other hand in apical views, the apex, commonly located in the near field of the probe, is usually blurred and the lateral wall is often poorly contrasted, yielding missing boundaries of significant size. In these cases, the multi-scale motion estimator based on monogenic signal captures texture information at a coarse scale which combined to the shape prior, allows to cope with this missing information and provides meaningful results but induces a lower accuracy. It can also be noted that the values obtained using the proposed method for the apical views are slightly lower than the inter-observer ones: here again the segmentation provides consistent results since the difference with the experts reference is comparable to the distance between experts.

The standard deviation for the epicardial border varies between 1.52×10^{-2} and 1.69×10^{-2} for D^* , 0.49 and 0.63 for the MAD and

1.1 and 1.65 for the HD. Though slightly higher, these values are in the same order as the standard deviation obtained for the experts outlined boundaries, showing that the segmentation results do not deviate from the mean value more than the experts' outlined boundaries do. The same conclusion can be drawn for the endocardial detection where the standard deviation varies between 1.85×10^{-2} and 2.51×10^{-2} for D^* , 0.36 and 0.66 for the MAD and 0.87 and 1.58 for the HD.

The figures provided in the last three columns of [Tables 4 and 5](#) allow comparing the performance of the proposed method and Hamou's method ([Hamou and El-Sakka, 2010](#)). The results show that our method yields better results (difference statistically significant at a level $p < 0.005$ for the Friedman rank test). Considering the mean differences between the error measures associated with the two approaches, D^* is on the average 6×10^{-2} (6.7×10^{-2}) lower, the MAD is 2.1 mm (1.6 mm) lower and the HD 4.6 mm (4.7 mm) lower which corresponds to at least a 50% (30%) improvement of the result for the epicardium (endocardium). This can be

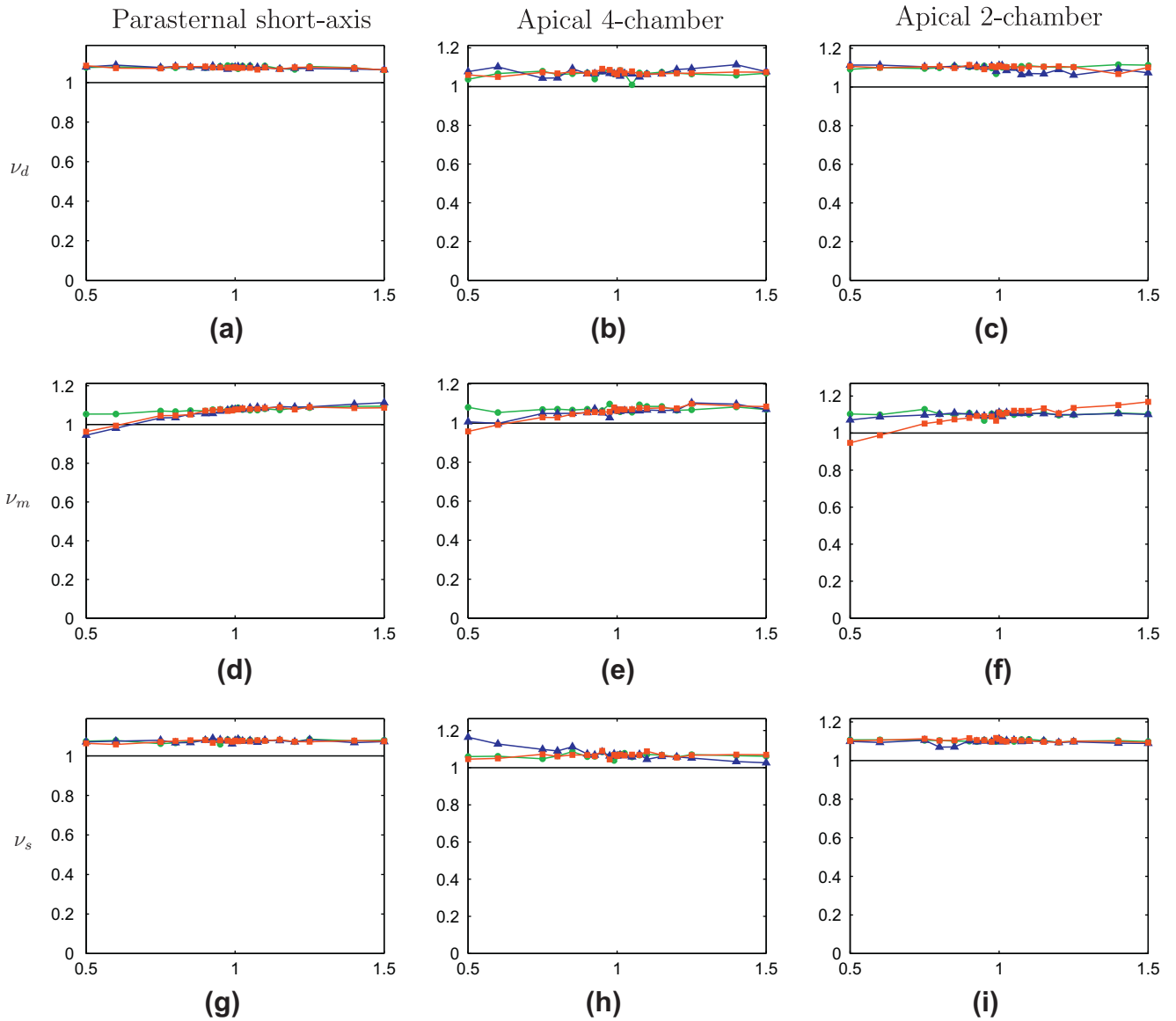


Fig. 8. Influence of the algorithm's parameters variation on the endocardial tracking performance. On the x-axis, 1 corresponds to the nominal value of the parameter and 0.5 (resp. 1.5) corresponds to a variation of -50% (resp. 50%) of the nominal value. Green: Data dominant region; Blue: Balanced region; Red: Shape dominant region. (For interpretation of the references to colour in this figure legend, the reader is referred to the web version of this article.)

explained by the fact that our motion term is more accurate than the classical OF hypothesis applied to B-mode images.

Tables 6 and 7 give the Williams Index (WI) and the 95% confidence interval (CI) for the epicardial and endocardial borders respectively. From these figures, we can see that except for the tracking of the epicardial border in parasternal short-axis views, the upper bound of the CI is always either higher than 1 or very close. This shows that our algorithm is able to produce results that differ from the manual references as much as they differ from one expert to the other. Regarding the results of tracking of the epicardium in parasternal short-axis views, several reasons can explain these values. First, we can note that the experts are really close to one another since the MAD value (0.77 mm) is halved when compared to apical views (1.5 and 1.54 mm) with a low standard deviation. The same trend can also be seen with the HD, showing that the experts agree with each other on both a global and local scale. Moreover, the mean difference between the IOD HD and the one obtained with our method is 0.7 mm which roughly corre-

sponds to one pixel (the mean pixel size of the dataset is equal to 0.58 mm/pixel).

Fig. 6 shows some of the worst tracking results and illustrates the difficulties encountered when tracking the myocardium. A problem corresponds to the missing boundaries that are frequent in apical views. For example in Fig. 6(b) and (d), the apex is blurred and part of the epicardium is out of the field of view. Thus no image or motion information can reliably drive the active contour, and

Table 8

Results of the segmentation on cardiac MRI sequences. The results of our method are shown in term of modified Dice criterion (D^*), Mean Absolute Distance (MAD) and Hausdorff distance (HD). The values are given as mean (Standard deviation). HD and MAD are given in mm.

	D^*	MAD	HD
Epicardium	3.2×10^{-2} (1.8×10^{-2})	1.05 (0.30)	3.28 (0.57)
Endocardium	6.1×10^{-2} (0.7×10^{-2})	1.29 (0.29)	3.58 (0.67)

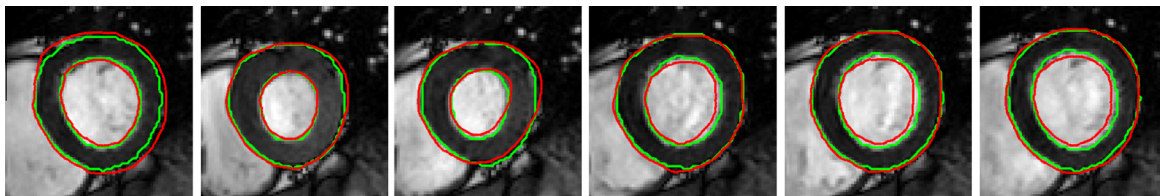


Fig. 9. Results of the tracking of the whole myocardium at 6 time points in the cardiac cycle in a cardiac MRI sequence. Green: experts reference; Red: our contour. (For interpretation of the references to colour in this figure legend, the reader is referred to the web version of this article.)

the contour evolves using only the shape prior. This, in turn, induces a lower accuracy.

6.4. Hyperparameters study

The stability of the proposed algorithm was tested by studying its robustness with respect to the variation of its parameters. The model parameters considered in this study were the 9 hyperparameters given in Table 1. The range where the parameter influence is evaluated was defined as a $\pm 50\%$ variation around the aforementioned optimal parameters values. The whole dataset was then segmented using the new value of one parameter while keeping the others fixed to their optimal value. Fig. 7 and 8 show the upper limit of the 95% confidence interval $WI_{95\%}$ for each parameter and for each view.

From these graphs, we can see that, except for the epicardial border in parasternal short-axis view, $WI_{95\%}$ is always either higher than or close to one and remains stable according to the variation of each of the parameters. This shows that the results from our algorithm differ from the manual references as much as the experts do. Moreover we can see that $WI_{95\%}$ is relatively constant when varying a parameter value from $\pm 50\%$ showing the robustness of our algorithm. This can be explained by the fact that in contrary to the methods where the weight is the same on the whole image, we only apply the hyperparameter locally. Thus a variation of this value only impacts a few segment of the myocardium, leaving the other segments unchanged.

6.5. Application to the segmentation of cardiac cine-MRI sequences

To show the generic nature of our motion prior term, the proposed algorithm was also applied on 10 short axis cardiac MRI sequences chosen randomly from the public dataset of the DETERMINE study (Kadish et al., 2009), available in the Cardiac Atlas Project platform (<http://www.cardiacatlas.org/>, Fonseca et al. (2011)). These sequences were acquired in different research center on 1.5T MRI (Philips Medical Systems Achieva or Intera and Siemens Avanto or Espree) and are based on steady-state free precession (SSFP) using a phased-array cardiac coil during repeated breath holds. The exams were performed on patients with coronary artery disease, mild-to-moderate left ventricle dysfunction and infarct size of 10% of LV mass. One expert manually outlined the myocardium on the whole dataset (225 images).

The proposed algorithm was then used to segment and track the myocardium on the whole dataset and the obtained results were compared to the manual reference. Table 8 provides the mean and standard deviation of the error measures obtained for the MRI data set on the epicardial and endocardial borders. Additionally, some tracking examples are shown in Fig. 9.

From this Table, we can see that the error measures are of the same order as the one obtained on US sequences. Moreover if we compare to the results reported in Table 3 of the review article of Petitjean and Dacher (2011), we can see that we perform better than most of the state of the art method (except for (Lelieveldt et al., 2001) for both borders and for (Lynch et al., 2006a,b; Barbari

et al., 2007) for the endocardial border only). This shows that our method is general enough to be able to handle both US and MRI cardiac sequences thanks to the motion prior and the spatially variable hyperparameters.

7. Conclusion

In this article, we have described a new motion prior energy that when minimized imposes a level consistency to the level-set function. This energy is then added to a recently proposed framework for the segmentation and tracking of the whole myocardium in multiple orientations. We have also proposed to take advantage of the anatomical and image properties of echocardiographic data to adjust the hyperparameters spatially in order to make the method more robust. The algorithm is then evaluated on a dataset of 15 sequences (≈ 900 images) where the manual references of two experts are available and compared favorably to another recent method (Hamou and El-Sakka, 2010) as well as on a dataset of 10 cine-MRI sequences to show its generic nature. We have also shown that our method was robust to variations of the hyperparameters. Future work will focus on the tracking of the myocardium in pathological cases and the extraction of clinical parameters (e.g. strain, strain rate).

Acknowledgment

This work was partially supported by Agence Nationale de la Recherche (US-Tagging Grant), the region Rhône-Alpes (ExploraDoc and AccueilDoc Grants) and Egide (PHC Tournesol Grant). This work was conducted in the framework of the LabEX PRIMES (“Physics Radiobiology Medical Imaging and Simulation”).

Appendix A. Derivation of the motion term

A.1. Notation

Let $\nabla\phi = \left(\frac{\partial\phi}{\partial x}, \frac{\partial\phi}{\partial y}, \frac{\partial\phi}{\partial t}\right)^T$ and $\mathbf{V} = (u, v, 1)^T$ be the estimated motion (in homogeneous coordinates), where T denotes the transposition.

In the following, the derivative will be noted as $f_x = \frac{\partial f}{\partial x}$. Let us also define the Hessian matrix of ϕ as

$$\mathcal{H}(\phi) = \begin{pmatrix} \phi_{xx} & \phi_{xy} & \phi_{xt} \\ \phi_{xy} & \phi_{yy} & \phi_{yt} \\ \phi_{xt} & \phi_{yt} & \phi_{tt} \end{pmatrix},$$

and the Jacobian matrix of \mathbf{V} as

$$\mathcal{J}(\mathbf{V}) = \begin{pmatrix} u_x & u_y & u_t \\ v_x & v_y & v_t \\ 0 & 0 & 0 \end{pmatrix}.$$

A.2. Derivation of the motion term

Let us recall the motion prior term (10):

$$\begin{aligned} E_m(\phi) &= \frac{1}{2} \int_{\Omega} \delta(\phi(\mathbf{p})) (\nabla \phi \cdot \mathbf{V})^2 d\mathbf{p} \\ &= \frac{1}{2} \int_{\Omega} \delta(\phi(\mathbf{p})) (\phi_t + u\phi_x + v\phi_y)^2 d\mathbf{p}. \end{aligned} \quad (\text{A.1})$$

The evolution equation of the level-set is obtained by deriving (A.1) with respect to ϕ using the Euler–Lagrange method (Gout et al., 2005). Considering a functional

$$E(\phi) = \int_{\Omega} L(x, y, t; \phi, \phi_x, \phi_y, \phi_t) d\mathbf{p}, \quad (\text{A.2})$$

its derivative with respect to ϕ is given by:

$$\frac{\partial E}{\partial \phi}(\phi) = \frac{\partial L}{\partial \phi} - \left(\frac{\partial}{\partial x} \frac{\partial L}{\partial \phi_x} + \frac{\partial}{\partial y} \frac{\partial L}{\partial \phi_y} + \frac{\partial}{\partial t} \frac{\partial L}{\partial \phi_t} \right). \quad (\text{A.3})$$

Here we have $L = \frac{1}{2} \delta(\phi) (\phi_t + u\phi_x + v\phi_y)^2 = \frac{1}{2} \delta(\phi) (\phi_t^2 + u^2 \phi_x^2 + v^2 \phi_y^2 + 2(u\phi_x \phi_t + v\phi_y \phi_t + uv\phi_x \phi_y))$. Thus

$$\frac{\partial L}{\partial \phi} = \frac{1}{2} \delta'(\phi) (\phi_t + u\phi_x + v\phi_y)^2 \simeq 0, \quad (\text{A.4})$$

$$\frac{\partial L}{\partial \phi_x} = \delta(\phi) (u^2 \phi_x + u\phi_t + uv\phi_y), \quad (\text{A.5})$$

$$\frac{\partial L}{\partial \phi_y} = \delta(\phi) (v^2 \phi_y + v\phi_t + uv\phi_x), \quad (\text{A.6})$$

$$\frac{\partial L}{\partial \phi_t} = \delta(\phi) (\phi_t + u\phi_x + v\phi_y) \quad (\text{A.7})$$

and

$$\begin{aligned} \frac{\partial}{\partial x} \frac{\partial L}{\partial \phi_x} &= \delta(\phi) (u^2 \phi_{xx} + u\phi_{xt} + uv\phi_{xy} + 2u_x u\phi_x + u_x \phi_t \\ &\quad + u_x v\phi_y + uv_x \phi_y), \end{aligned} \quad (\text{A.8})$$

$$\begin{aligned} \frac{\partial}{\partial y} \frac{\partial L}{\partial \phi_y} &= \delta(\phi) (v^2 \phi_{yy} + v\phi_{yt} + uv\phi_{xy} + 2v_y v\phi_y + v_y \phi_t \\ &\quad + u_y v\phi_x + uv_y \phi_x), \end{aligned} \quad (\text{A.9})$$

$$\frac{\partial}{\partial t} \frac{\partial L}{\partial \phi_t} = \delta(\phi) (\phi_{tt} + u\phi_{xt} + v\phi_{yt} + u_t \phi_x + v_t \phi_y). \quad (\text{A.10})$$

where the assumption is made that $\frac{\partial}{\partial \phi} \delta(\phi) \simeq 0$ near the zero-level and thus should not affect the evolution process (as in Lankton and Tannenbaum, 2008).

The derivative of (A.1) with respect to ϕ thus writes

$$\begin{aligned} \frac{\partial E_m}{\partial \phi}(\phi) &= -\delta(\phi) (u^2 \phi_{xx} + u\phi_{xt} + uv\phi_{xy} + 2u_x u\phi_x + u_x \phi_t \\ &\quad + u_x v\phi_y + uv_x \phi_y + v^2 \phi_{yy} + v\phi_{yt} + uv\phi_{xy} \\ &\quad + 2v_y v\phi_y + v_y \phi_t + u_y v\phi_x + uv_y \phi_x + \phi_{tt} + u\phi_{xt} \\ &\quad + v\phi_{yt} + u_t \phi_x + v_t \phi_y) \end{aligned} \quad (\text{A.11})$$

$$\begin{aligned} \frac{\partial E_m}{\partial \phi}(\phi) &= -\delta(\phi) (u^2 \phi_{xx} + 2uv\phi_{xy} + v^2 \phi_{yy} + 2u\phi_{xt} + 2v\phi_{yt} \\ &\quad + \phi_{tt} + u(u_x \phi_x + v_x \phi_y) + v(u_y \phi_x + v_y \phi_y) + u_t \phi_x \\ &\quad + v_t \phi_y + (u_x + v_y)(\phi_t + u\phi_x + v\phi_y)). \end{aligned} \quad (\text{A.12})$$

$$\frac{\partial E_m}{\partial \phi}(\phi) = -\delta(\phi) \left(\mathbf{V}^T \mathcal{H}(\phi) \mathbf{V} + \nabla \phi^T \mathcal{J}(\mathbf{V}) \mathbf{V} + \text{Tr}(\mathcal{J}(\mathbf{V})) \nabla \phi^T \mathbf{V} \right), \quad (\text{A.13})$$

where $\text{Tr}(\mathcal{J}(\mathbf{V}))$ denotes the trace of the matrix $\mathcal{J}(\mathbf{V})$.

The evolution equation is then given by:

$$f_m = \frac{\partial \phi}{\partial \tau} = -\frac{\partial E_m}{\partial \phi} = \delta(\phi) \left(\mathbf{V}^T \mathcal{H}(\phi) \mathbf{V} + \nabla \phi^T \mathcal{J}(\mathbf{V}) \mathbf{V} + \text{Tr}(\mathcal{J}(\mathbf{V})) \nabla \phi^T \mathbf{V} \right) \quad (\text{A.14})$$

where τ is an artificial time parameter (that does not correspond to the “real” time dimension t).

References

- Alessandrini, M., Basarab, A., Liebgott, H., Bernard, O., 2013. Myocardial motion estimation from medical images using the monogenic signal. *IEEE Trans. Image Process.* 22 (3), 1084–1095.
- Berbari, R.E., Bloch, I., Redheuil, A., Angelini, E., E.Mousseaux, Frouin, F., Herment, A., 2007. An automated myocardial segmentation in cardiac MRI. In: *IEEE Eng. Med. Biol. Soc.*, pp. 4508–4511.
- Bosch, J., Mitchell, S., Lelieveldt, B., Nijland, F., Kamp, O., Sonka, M., Reiber, J., 2002. Automatic segmentation of echocardiographic sequences by active appearance motion models. *IEEE Trans. Med. Imag.* 21, 1374–1383.
- Brox, T., Bruhn, A., Weickert, J., 2006. Variational motion segmentation with level sets. In: *European Conference on Computer Vision (ECCV'06)*. Graz, Austria, pp. 471–483.
- Brox, T., Rosenhahn, B., Gall, J., Cremers, D., 2010. Combined region and motion-based 3d tracking of rigid and articulated objects. *IEEE Trans. Pattern Anal. Machine Intell.* 32 (3), 402–415.
- Bruhn, A., Weickert, J., 2006. Confidence measures for variational optic flow methods. In: *Geometric Properties from Incomplete Data*, pp. 283–297.
- Carneiro, G., Nascimento, J., Freitas, A., 2012. The segmentation of the left ventricle of the heart from ultrasound data using deep learning architectures and derivative-based search methods. *IEEE Trans. Image Process.* 21 (3), 968.
- Casero, R., Noble, J., 2008. A novel explicit 2d+1 cyclic shape model applied to echocardiography. In: *Medical Image Computing and Computer-Assisted Intervention (MICCAI'2008)*, pp. 527–534.
- Cerqueira, M., Weissman, N., Dilsizian, V., Jacobs, A., Kaul, S., Laskey, W., Pennell, D., Rumberger, J., Ryan, T., Verani, M., 2002. Standardized myocardial segmentation and nomenclature for tomographic imaging of the heart. *Circulation* 105, 539–542.
- Chalana, V., Kim, Y., 1997. A methodology for evaluation of boundary detection algorithms on medical images. *IEEE Trans. Med. Imag.* 16 (5), 642–652.
- Chalana, V., Linker, D., Haynor, D., Kim, Y., 1996. A multiple active contour model for cardiac boundary detection on echocardiographic sequences. *IEEE Trans. Med. Imag.* 15 (3), 290–298.
- Chan, T., Vese, L., 2001. Active contours without edges. *IEEE Trans. Image Process.* 10, 266–277.
- Comaniciu, D., Zhou, X.S., Krishnan, S., 2004. Robust real-time myocardial border tracking for echocardiography: an information fusion approach. *IEEE Trans. Med. Imag.* 23, 849–860.
- Cremers, D., 2006. Dynamical statistical shape priors for level set-based tracking. *IEEE Trans. Pattern Anal. Machine Intell.* 28, 1262–1273.
- Cremers, D., Soatto, S., 2005. Motion competition: a variational approach to piecewise parametric motion segmentation. *Int. J. Comput. Vis.* 62, 249–265.
- Dias, J.M.B., Leitao, J.M.N., 1996. Wall position and thickness estimation from sequences of echocardiographic images. *IEEE Trans. Med. Imag.* 15, 25–38.
- Dice, L., 1945. Measures of the amount of ecologic association between species. *Ecology* 26, 297–302.
- Dietenbeck, T., Alessandrini, M., Barbosa, D., D'hooge, J., Friboulet, D., Bernard, O., 2012. Detection of the whole myocardium in 2d-echocardiography for multiple orientations using a geometrically constrained level-set. *Med. Image Anal.* 16, 386–401.
- Dietenbeck, T., Barbosa, D., Alessandrini, M., Jasaityte, R., Rosebyn, V., D'hooge, J., Bernard, O., Friboulet, D., 2013. Multiview myocardial tracking in echocardiographic 2d sequences using shape and motion constrained level-set. In: *IEEE International Symposium on Biomedical Imaging (ISBI'13)*. San Francisco, California, USA, pp. 1010–1013.
- Duan, Q., Angelini, E., Laine, A., 2010. Real-time segmentation by active geometric functions. *Comput. Methods Programs Biomed.* 98 (3), 223–230.
- Ehrhardt, J., Schmidt-Richberg, A., Handels, H., 2008. Simultaneous segmentation and motion estimation in 4D-CT data using a variational approach. In: *SPIE Medical Imaging Conference*.
- Felsberg, M., Sommer, G., 2001. The monogenic signal. *IEEE Trans. Signal Process.* 49 (12), 3136–3144.
- Fonseca, C., Backhaus, M., Bluemke, D., Britten, R., Chung, J., Cowan, B., Dinov, I., Finn, J., Hunter, P., Kadish, A., Lee, D., Lima, J., Medrano-Gracia, P., Shivkumar, K., Suinesiaputra, A., Tao, W., Young, A., 2011. The cardiac atlas project – an imaging database for computational modeling and statistical atlases of the heart. *Bioinformatics* 27 (16), 2288–2295.
- Gout, C., LeGuyader, C., Vese, L., 2005. Segmentation under geometrical conditions using geodesic active contours and interpolation using level set methods. *Numer. Algor.* 39, 155–173.
- Hamou, A., El-Sakka, M., 2010. Optical flow active contours with primitive shape priors for echocardiography. *EURASIP J. Adv. Signal Process.*, 2010.
- Herbulot, A., Jehan-Besson, S., Duffner, S., Barlaud, M., Aubert, G., 2006. Segmentation of vectorial image features using shape gradients and information measures. *J. Math. Imag. Vis.* 25, 365–386.
- Huttenlocher, D., Klanderman, G., Rucklidge, W., 1993. Comparing images using the Hausdorff distance. *IEEE Trans. Pattern Anal. Machine Intell.* 15 (9), 850–863.
- Jacob, G., Noble, J., Mulet-Parada, M., Blake, A., 1999. Evaluating a robust contour tracker on echocardiographic sequences. *Med. Image Anal.* 3 (1), 63–75.
- Kadish, A., Bello, D., Finn, J., Bonow, R., Schaechter, A., Subacius, H., Albert, C., Daubert, J., Fonseca, C., Goldberger, J., 2009. Rationale and design for the

- defibrillators to reduce risk by magnetic resonance imaging evaluation (DETERMINE) trial. *J. Cardiovasc. Electrophysiol.* 20 (9), 982–987.
- Kohlberger, T., Cremers, D., Rousson, M., Ramaraj, R., Funka-Lea, G., 2006. 4d shape priors for a level set segmentation of the left myocardium in spect sequences. In: *Medical Image Computing and Computer-Assisted Intervention (MICCAI'06)*, pp. 92–100.
- Lankton, S., Tannenbaum, A., 2008. Localizing region-based active contours. *IEEE Trans. Image Process.* 17, 2029–2039.
- Lelieveldt, B., Mitchell, S., Bosch, J., van der Geest, R., Sonka, M., Reiber, J., 2001. Time-continuous segmentation of cardiac image sequences using active appearance motion models. In: *Information Processing in Medical Imaging: 17th International Conference (IPMI'01)*, LNCS, Davis, CA, USA, pp. 446–452.
- Leung, K., Danilouchkine, M., van Stralen, M., de Jong, N., van der Steen, A., Bosch, J., 2011. Left ventricular border tracking using cardiac motion models and optical flow. *Ultrasound Med. Biol.* 37 (4), 605–616.
- Lynch, M., Ghita, O., Whelan, P., 2006a. Automatic segmentation of the left ventricle cavity and myocardium in MRI data. *Comput. Biol. Med.* 36 (4), 389–407.
- Lynch, M., Ghita, O., Whelan, P., 2006b. Left-ventricle myocardium segmentation using a coupled level-set with a priori knowledge. *Comput. Med. Imag. Graph.* 30 (4), 255–262.
- Lynch, M., Ghita, O., Whelan, P., 2008. Segmentation of the left ventricle of the heart in 3-D+t MRI data using an optimized nonrigid temporal model. *IEEE Trans. Med. Imag.* 27, 195–203.
- Nascimento, J., Marques, J., 2008. Robust shape tracking with multiple models in ultrasound images. *IEEE Trans. Image Process.* 17 (3), 392–406.
- Noble, J.A., Boukerroui, D., 2006. Ultrasound image segmentation: a survey. *IEEE Trans. Med. Imag.* 25 (11), 987–1010.
- Orderud, F., Kiss, G., Torp, H.G., 2008. Automated coupled segmentation of endo- and epicardial borders in 3D echocardiography. In: *IEEE International Ultrasonics Symposium (IUS'08)*, Beijing, China, pp. 1749–1752.
- Osher, S., Fedkiw, R., 2002. *Level Set Methods and Dynamic Implicit Surfaces*. Springer Verlag.
- Osher, S., Sethian, J., 1988. Fronts propagating with curvature-dependent speed: algorithms based on Hamilton–Jacobi formulation. *J. Comp. Phys.* 79, 12–49.
- Papin, C., Boutheimy, P., Mémin, E., Rochard, G., 2000. Tracking and characterization of highly deformable cloud structures. In: *European Conference on Computer Vision (ECCV'00)*, LNCS, vol. 1843, pp. 428–442.
- Petitjean, C., Dacher, J.-N., 2011. A review of segmentation methods in short axis cardiac MR images. *Med. Image Anal.* 15, 169–184.
- Sussman, M., Fatemi, E., Smereka, P., Osher, S., 1998. An improved level set method for incompressible two-phase flows. *J. Comput. Fluids* 27, 663–680.
- Unal, G., Krim, H., Yezzi, A., 2005. Fast incorporation of optical flow into active polygons. *IEEE Trans. Image Process.* 14 (6), 745–759.
- Zhang, Q., Pless, R., 2005. Segmenting cardiopulmonary images using manifold learning with level sets. In: *Computer Vision for Biomedical Image Appl.*, LNCS, vol. 3765, pp. 479–488.
- Zhou, X., Comaniciu, D., Gupta, A., 2005. An information fusion framework for robust shape tracking. *IEEE Trans. Pattern Anal. Machine Intell.* 27, 115–129.
- Zhou, X., Comaniciu, D., Krishnan, S., 2004. Coupled-contour tracking through non-orthogonal projections and fusion for echocardiography. In: *European Conference on Computer Vision (ECCV'04)*, Czech Republic, pp. 336–349.
- Zhu, Y., Papademetris, X., Sinusas, A.J., Duncan, J.S., 2010. A coupled deformable model for tracking myocardial borders from real-time echocardiography using an incompressibility constraint. *Med. Image Anal.* 14, 429–448.